small structures
www.small-structures.com

Programmable Functional Connectivity and Synchronous Activity in Resistive Switching Self-Assembled Nanostructured Networks

Davide Decastri, Thierry Nieus, Cristina Zuccali, Flavio Giacomozzi, Leandro Lorenzelli, Francesca Borghi, and Paolo Milani*

The efficiency of biological data processing systems is based on their adaptive connectivity and on the mutual interactions of their elements at different scales. These features are not substantially present in the design of electronic architectures based on conventional integrated circuits. The exploitation of self-assembled systems characterized by nonlinear dynamics is actively investigated as a viable alternative strategy to develop energy-efficient data processing devices. However, the encoding of external stimuli and the decoding of information from the analog response of such systems is still a challenge. Here we characterize the functional connectivity and the synchronicity between active sites in cluster-assembled nanostructured Au films showing resistive switching behavior by a combined approach based on micro-thermography and electrical measurements. We investigate the complex mechanisms involved in the network reorganization leading to its resistive switching activity and we identify the interplay between network dimensions and its emerging electrical behavior. We investigate the control on the synchronous activity and on the connectivity of the micrometric active sites which rule the emerging network dynamics and determe the performance of data processing devices. This activity is described using data analysis techniques commonly used in neuroscience, which are proposed for the first time to characterize neuromorphic systems.

1. Introduction

The rapidly growing demand for computational power of electronic devices, prompted by the widespread AI-based applications in our all-day-life,[1] is not adequately supported by energy-sustainable solutions due to the lack of hardware architectures escaping from the limitations of the von Neuman bottleneck.

Alternatives in terms of sustainability can be taken from biological models and, in particular, from the mammalian brain that is characterized by outperforming efficient data processing capabilities emerging from a complex wiring of interconnected neurons, interacting and adapting at different scales in response to external stimuli.[2–4] These systems are based on a redundant and adaptive neuronal network activity, in which the structural and functional organization of neural network at different scales mutually influence each other and result into complex emerging behaviors.[3,4]

In mammalian brains, individual neurons count for little; it is population activity that matters.[5,6] Recurrently connected networks of spiking neuronal cells underpin the astounding information processing capabilities of the brain, which can learn through synaptic plasticity to carry out complex network computations. Part of the difficulty in understanding population coding is that neurons are noisy, which means that the same pattern of activity never occurs twice, even when the same stimulus is presented.[5] In this context, correlation and simultaneity within spiking activity of different neurons may play a crucial role in decreasing/increasing the amount of information that is decoded by population activity, in a nontrivial way.[5]

Since neural cells are recurrently connected, forming a certain number of recursive loops, their own connectivity plays a crucial role in the coordinated and synchronous firing of the population.[7] In vivo, waves of spikes transiently characterize the activity of developing brain circuits and are fundamental for activity-dependent circuit formation.[8,9] Interestingly, neurons in vitro can also self-organize and rewire to form networks[10] that spontaneously express a rich repertoire of coordinated spiking activity after a few weeks of growth. Collective spiking patterns, referred to as network bursts[11] in which most neurons in the network fire

D. Decastri, C. Zuccali, F. Borghi, P. Milani
CIMaINa and Department of Physics "Aldo Pontremoli"
University of Milano
via Celoria 16, 20133 Milano, Italy
E-mail: francesca.borghi@unimi.it

T. Nieus
Department of Environmental Science and Policy
University of Milano
via Celoria 10, 20133 Milano, Italy

F. Giacomozzi, L. Lorenzelli
Sensors and Devices Center
Fondation Bruno Kessler
Via Sommarive 18, 38123 Trento, Italy

The ORCID identification number(s) for the author(s) of this article can be found under https://doi.org/10.1002/sstr.202500330.

DOI: 10.1002/sstr.202500330

together,[12] can rather persist over time, lasting up to a few months.[13] Particular local connectivity plays a crucial role in the upcoming of network bursts.[14] Moreover, it has been shown that the same regions carry most of the state-dependent information about external stimuli and undergo plastic reorganization affecting how the network bursts propagate in the network.[6,15]

Although from a biological point of view, the mechanisms of stimuli and information encoding/decoding in neuronal populations and the role of noise are still a matter of investigation, the exploitation of artificial systems based on self-assembled materials, emulating the complex and adaptive structure of the brain for data processing, is actively studied.[16–20] In particular, the exploitation of the emerging behavior at different scales in complex self-assembled artificial systems is a strategy that could lead to a more efficient data processing,[21,22] and possibly to the advent of a new concept of in materia computation.[17,21] The main physical phenomena driving nonlinear electrical behaviors and memory effects in self-assembled systems are the formation/destruction of metallic filaments between nanowires[18,23,24] or through insulating shell around metallic nanoparticles,[25,26] as also the reorganization of grain boundaries at the junctions of a nanogranular metallic structure.[27–29] Self-assembled networks of nanoparticles and nanowires have been exploited for physical reservoir computing,[17,30] for nonlinear transformation tasks,[31,32] and as Boolean functions classifier.[19] To reach this goal, the characterization of the activity of self-assembled systems at different scales and the control over it through proper stimuli and feedback loops are of fundamental importance.

Accessing information about the dynamics that produce the complex electrical behavior such as resistive switching (RS) activity in self-assembled nanostructured systems is challenging for several reasons. Electrical resistivity tomography (ERT) analysis has been developed[33,34] to allow the mapping of electrical conductivity in self-assembled networks. However, ERT algorithm is based on linear approximation of the electric characteristics, thus it fails in case of strong nonlinearity or anisotropy in local electric conduction. Furthermore, the local solution reconstructed with finite element method algorithm becomes increasingly inaccurate as the distance from the electrodes grows, and the results are affected by the meshing procedure. Lock-in thermography has also been used to describe the change in conductance pathway characterizing random-assembled Ag–TiO_2 nanowire network.[35] However, the control on network dynamic was not achieved, and the work is rather on selective modification of the conductive scenario, without a programmable protocol and a systematic approach.

Here, we propose a strategy based on micro-thermography and electrical measurements, for the study of the spatial and temporal dynamics of the resistive switching activity of a nanostructured gold network.[36] Cluster-assembled films produced by supersonic cluster beam deposition (SCBD)[37] have been widely studied both experimentally[27,36,38–42] and theoretically,[29,43] as resistive switching systems that can be used for neuromorphic data processing tasks.[19,20] The main mechanism responsible for their electrical conductivity behavior is the stochastic reorganization of the grain boundaries of gold cluster-assembled films,[29,40,42,43] driven principally by electromigration and Joule heating.

Furthermore, we describe the adaptive reorganization of the nanostructured network, from the nano to the macro scale, along with all those strategies used to control the network connectivity, the synchronicity, and correlation of activities emerging in different micrometric sites of the nanostructured network, which promote its overall resistive switching electrical response. A network correlation coefficient, describing the activity of local micrometric sites, is adopted according to an approach typical of neuroscience.

2. Experimental Section

2.1. Nanostructured Thin Film Production

Nanostructured gold films (ns-Au) have been deposited via SCBD[37,44–46] between two sputtered gold electrodes (100 nm thick) on glass substrate; lift-off methods of photoresist masks have been used to obtain the suitable lateral resolution of the films (**Figure 1**a). Cluster-assembled nanostructured films are highly porous and disordered, resulting from the stacking of nanoparticles according to ballistic deposition principles.[47] The nanostructured films are formed by nanometric cubic phase Au clusters,[41] characterized by a bimodal distribution,[39,47] with very small aggregates peaked at 0.40 nm and a population of the largest clusters around 6 nm. A further detailed structural characterization of the pristine ns-Au, by means of X-ray photoelectron spectroscopy, has already been provided in ref. [48]. Gold cluster-assembled films have been deposited beyond the electrical percolation threshold (thickness about 10–20 nm).

The main steps of sample fabrication are summarized in Figure 1a. We produced nanostructured gold thin films with different dimensions to investigate the role of the film dimensions in the emerging of the complex electrical behavior. Specifically, the size of the edge parallel to the overall current direction, i.e., the length (that corresponds to the distance between the electrodes), ranges from 125 μm to 1 mm, and the size of the edge perpendicular to the current direction, i.e., the width, ranges from 125 μm to 2 mm (see the sketch in Figure 1c for reference).

2.2. Micro-Thermographic and Electrical Measurements

We used an uncooled micro-bolometric thermal camera (Flir A655sc, NETD 30 mK) equipped with close-up lens (Instantaneous Field of View, IFOV 25 μm) for thermal imaging of the ns-Au samples during electrical stimulation (a schematic is shown in Figure 1b). Videos were recorded at 50 Hz. Electric stimulation and measurements (application of constant voltage/bias) have been performed using a Keithley 2606B SMU, with sampling frequency of 20 Hz.

Glass is a good electrical insulator substrate, with also both low thermal conductivity ($\approx 1 \frac{W}{K \cdot m}$) and low specific heat ($\approx 840\ J\ g^{-1}\ K^{-1}$). Low thermal conductivity allows to reduce heat diffusion through the sample and to localize precisely the areas involved in RS of the ns-Au above it. Low specific heat allows to have fast thermal transients,[49] and consequently, to obtain good temporal responsivity.

As-deposited ns-Au thin films are ohmic conductors and show linear electrical properties. After a proper electric stimulation was provided (i.e., current flowing is high enough), ns-Au films undergo structural modifications over the entire nanostructured network triggered by different physical mechanisms (thermally promoted dewetting and electromigration) well described in refs. [36,42], and RS activity is triggered. We call this process

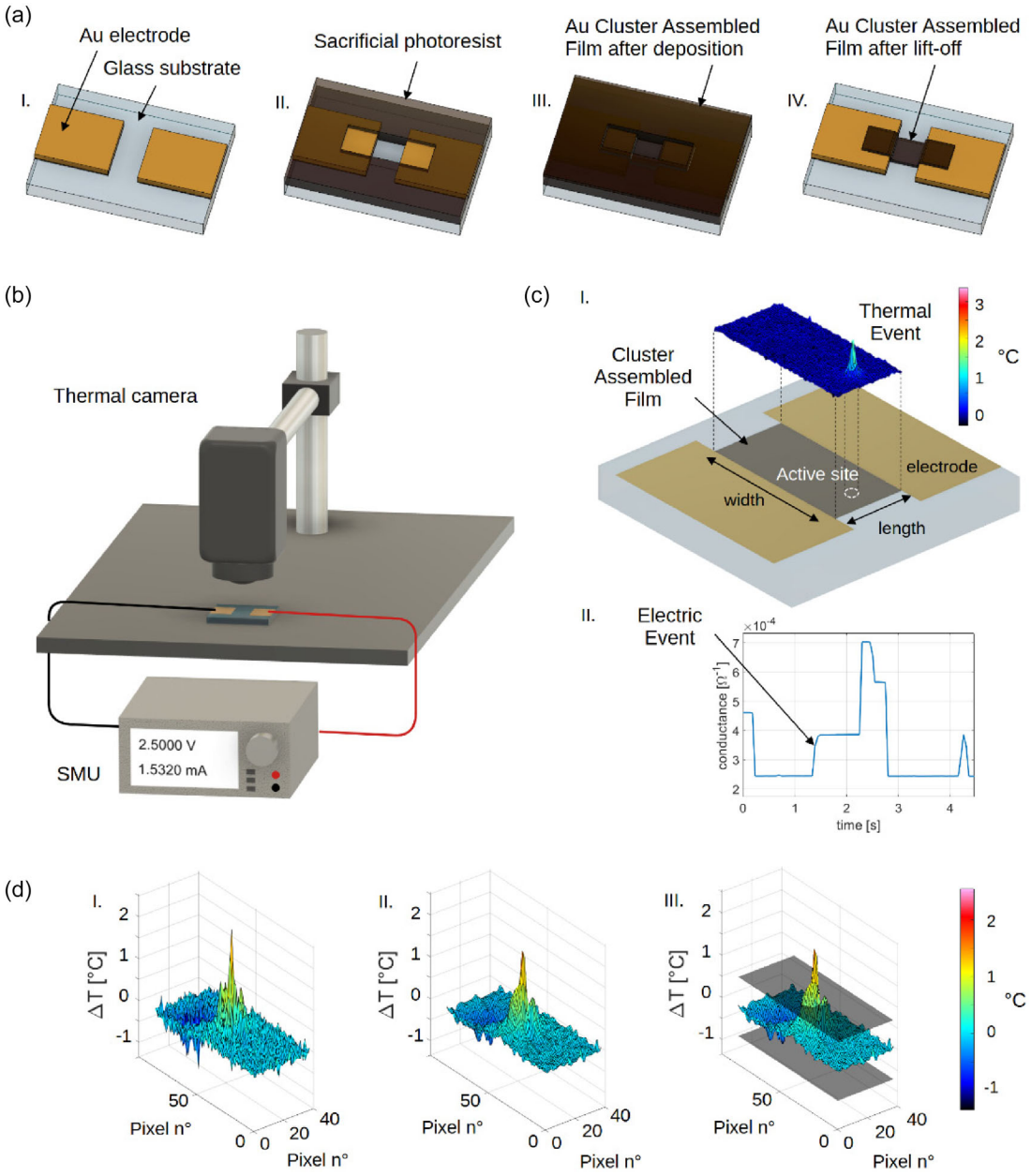

Figure 1. a) Schematic representation of the main steps in ns-Au thin film microfabrication. After electrodes deposition and lithography, a sacrificial layer of photoresist was applied. Gold nanostructured film is deposited by means of SCBD, and photoresist lift-off was accomplished by acetone immersion. b) Schematic representation of the experimental setup. Electric measurement and IR images were collected by a computer for data analysis. c) Schematics of the samples and figurative summary of the vocabulary. d) Examples of analysis performed by the TE recognition algorithm. Surface representation is adopted to highlight the effects of denoising. (I) Differential image of consecutive frames (II), same image in (I) after smoothing, (III) thresholding process for TE recognition.

electric forming process.[36] This procedure was carried out by stimulating ns-Au films at constant bias for 1 min, and, in absence of the expected abrupt increase in electrical resistance, a further stimulation was provided, increasing the applied bias. Since different ns-Au geometries were explored, we chose the voltage step between two subsequent stimulations to keep the variation of the mean electric field constant to $2 \times 10^3\ \mathrm{V\,m^{-1}}$. This strategy allowed to have uniformity in the forming processes, irrespective of the sample dimensions.

We have already demonstrated how the forming process and the resulting resistive switching activity do not depend on the gold pristine cluster size.[47]

2.3. Identification of Thermal Events

Electric stimulations at constant bias were performed after forming, as described in ref. [27], to explore the resistive switching activity of the gold nanostructured network. After forming, the

electric conduction of the ns-Au thin film was no more uniform: regions with much higher current density respect to the surrounding were often detectable by micro-thermography in the form of "hotspots", due to local joule heating effect. During a constant voltage stimulation lasting few minutes, hotspots can change their temperature, and new hotspots appear in different regions of the nanostructured network (a video acquired by micro-thermography of a ns-Au activity during electrical measurement is available in Supporting Information).

To describe this rich phenomenology, we adopted the following vocabulary (reported graphically in Figure 1c): conductance variations detected by means of electric measurements were referred as "electric events" (EEs). Here, we referred to "thermal events" (TEs) to indicate significant (compared to noise, see in the following paragraph an in-depth discussion) temperature variations detected along the ns-Au. Since thermal image provided also spatial information about TEs, we defined "active site" (AS) any location where one or more TEs have been detected. The notion of AS is strongly related to our spatial resolution (about 25 μm) because we did not have the possibility to distinguish features on scales below thermal camera IFOV.

EEs have been detected comparing absolute conductance variations with multiples of noise standard deviation (see ref. [27] for further details). As we did for EEs detection, we used an analogous algorithm for automatic TEs detection in thermal images (Figure 1d). MATLAB environment was used to develop the software. In this case, we performed pixel-by-pixel difference (in short, a time derivative[50]) between frames 40 ms apart (we call this "differential time series") because this is the typical time scale on which thermal transients take place in our systems. We processed the image that has been obtained by difference, performing denoising using 2D discrete wavelet transform (DWT) and reconstruction by means of a first-level low-pass filter. This step allows to effectively smooth random temperature variations with high spatial frequency that are mostly due to electronic noise, sensor instability, and nonstationary environmental conditions. Furthermore, DWT reconstruction allows to enhance the importance of temperature variations taking place on broad length-scales, that are likely to be actual TEs, due to the expected heat diffusion along the ns-Au and the substrate. TEs were then detected by means of simple thresholding: if the modulus of the maximum temperature variation exceeded a threshold, a TE was detected. The threshold of 0.7 K was fixed considering both the standard deviation of the noise, that has been estimated to be of the order of 0.1 K (but can slightly vary between noise equivalent temperature difference (NETD) and 0.15 K, depending on the stability of atmospheric condition and camera warmup period), by analyzing the temperature fluctuations in the thermal images in absence of electric stimuli, and the presence of spurious thermal transients along the ns-Au films after most intense TEs, that can produce erroneous event detection.

2.4. Spatial Occurrence of the Thermal Events

We used principal component analysis (PCA)[51,52] as a data mining technique to extract features from our recordings. PCA is an unsupervised learning algorithm for dimensionality reduction based on the search of linear combinations of variables that better accounts for the variance in a dataset. The first step of PCA consists in diagonalizing the covariance matrix and describing the dataset in the basis of PCs. This procedure is generally profitable because it allows to effectively detect a small subset of PCs (i.e., linear combinations of the experimental outcomes) that accounts for most of the data dispersion. In the second instance, it is possible to reduce the dimensionality of the data, by excluding less informative PCs, i.e., those associated with the smallest eigenvalues.

From the perspective of this study, each frame represents a set of coordinates in a space with dimensionality equal to the number of pixels, while the collection of frames composing the recording is the experimental dataset. The idea behind the application of this strategy is the following: if some features (e.g., systematic temperatures variations occurring simultaneously in a specific set of pixels) are present in the dataset, they are responsible for the spreading of data along specific directions in the experimental domain. For this reason, we expect that due to the presence of TEs, the pixels framing ASs produce highly spread readings respect to other pixels and can be effectively detected by means of PCA. The reader must be very careful to notice that PCA is not a clustering technique, and furthermore, it assumes only the first two moments of the data distribution (i.e., mean and variance) to be nonzero. PCA tends to be inefficient if data distribution presents very complicated features,[51] that necessitate nonzero higher-order moments to be accurately described. For this reason, it can happen that multiple directions of large variance are mixed (see ref. [51]). Our main goal in using PCA is to perform dimensionality reduction to highlight, through AS detection, the possible existence of few stereotyped dynamics in our system.

2.5. Correlation Index of Active Site Activities

Here, we describe the spike time tiling coefficient (STTC),[53] usually adopted to measure correlation and synchronicity in neuronal activity, and here adapted for the description of RS activity taking place in different active sites (ASs). The main assumption of STTC is that the spiking pattern is stationary.[53] This was addressed in this nonbiological system by calculating it over long RS activity traces, acquired at the lowest possible bias, to ensure accurate STTC assessment in steady resistive switching regimes.

Considering a recording of duration T and given one AS A, where a number of N_A thermal events (TEs) have been detected, the time instants where TEs happen in A, $0 \leq t_i^A \leq T$ with $i = 1, \ldots, N_A$, and a synchronicity window Δt, we define:

$$\tilde{T}_A = \left\{ \bigcup_{i=1}^{N_A} [t_i^A - \Delta t, t_i^A + \Delta t] \right\} \cap [0, T] \quad (1)$$

i.e., the set of all time instants "in proximity" (according to the synchronicity window) to any TE happening in A during the recording, and thus "available" for a coordinated activity with B. Note also that $\tilde{T}_A$ is defined by considering intervals starting before TEs in A. This in not conflicting with causality principle but instead accounts for the possibility that events in B trigger events in A.

We use $\tilde{T}_A$ to define two other important quantities. At first, we define:

$$T_A = \frac{\lambda(\tilde{T}_A)}{T} \tag{2}$$

where $\lambda(\tilde{T}_A)$ denotes the Lebesgue measure of $\tilde{T}_A$. Roughly speaking, T_A represents the fraction of time that is "occupied" by the activity detected in A.

Given another AS B, we define:

$$P_A(B) = \frac{|\{t_i^B : t_i^B \in \tilde{T}_A, i = 1, \ldots, N_B\}|}{N_B} \tag{3}$$

where the notation $||$ represents set cardinality. $P_A(B)$ is the fraction of TEs in B that happen simultaneously to any TE in A, according to the synchronicity window Δt (i.e., happen within $\pm\Delta t$ from at least one TE in A). If the recording period is sufficiently long, both T_A and $P_A(B)$ can be regarded as probabilities.

The basic idea behind STTC is the following: supposed to know the dynamics that is likely to produce the correlations and thus to be able to set a reasonable value for Δt (or, at least, to set an upper bound to Δt) and considering a sufficiently long recording period, if the activity in A is completely uncorrelated to the activity in B, then it should be $P_A(B) = T_A$. On the contrary, if activities in A and B tend to be positively correlated, we expect that $P_A(B) > T_A$. Similarly, in case of anticorrelation $P_A(B) < T_A$.

By using the quantities that have been defined above, STTC has the form:

$$\mathrm{STTC} = \frac{1}{2}\left(\frac{P_B(A) - T_B}{1 - P_B(A)T_B}\right) + \frac{1}{2}\left(\frac{P_A(B) - T_A}{1 - P_A(B)T_A}\right) \tag{4}$$

STTC is defined to fulfil symmetry with respect to A and B, and the normalization ensures that it is bounded between $\mathrm{STTC} = -1$ (fully negatively correlated) and $\mathrm{STTC} = 1$ (fully positively correlated).

Despite STTC is widely used to study biological neuronal cultures,[54–56] to our knowledge, this is the first attempt to perform this kind of analysis on a nonbiological system. We chose this coefficient to provide an estimate of the correlation and synchronicity in RS traces since, compared to other possible metrics, it has been shown to be independent from the typical firing rate of the system.[53] Note that Δt is the only free parameter of the model; this allows to evaluate pairwise correlation in RS activity recorded in different ASs within a sliding window, to be informative about correlation timescale. In fact, this parameter can be set a-priori if the timescales of the physical (or biological) mechanisms that lead to interactions are known. In the absence of a physical hypothesis it can be varied to check the presence of typical timescales of correlation.[53] Due to the lack of precise information regarding the physics that could drive interactions in our system, we followed the second strategy. STTC was computed varying Δt ranging over two orders of magnitude: from 0.02 s (i.e., thermal camera sampling period) to 20 s (sufficiently lower than the sampling period, i.e., 300 s). By increasing the synchronicity window, i.e., assuming the presence of interactions on long time scales, we expect that coordination increases.

We also provide an estimation of the firing rate in TE temporal series corresponding to single ASs. Assuming the presence of a bursting RS activity in correspondence of single ASs (our findings support this assumption, see Section 3), we adopted the method described in ref. [53] to identify bursts and then we estimate inter switch intervals (ISIs) inside bursts. The method for burst detection is adaptive, i.e., it identified bursts without a priori knowledge of ISIs timescales, and it relied on the statistics of the time series itself. It consisted in the separation between short ISIs (most probably belonging to bursts) and long ISIs (linked to silence periods, i.e., intra-burst intervals) through a comparison with ISIs mean. The procedure is repeated over the set of short ISIs to exclude all intra-burst intervals with high confidence.

3. Results and Discussion

3.1. Forming Process

We characterized the forming process of ns-Au films with length 1 mm and width 2 mm. During the forming process, heat is dissipated through the glass substrate and along ns-Au films, as also on the gold electrodes. The temperature profile along the direction of the current flow presented a smooth peak roughly in correspondence to the center of the conductive film, as expected and described in refs. [57–59]. After forming, we observed a significant decrease of radiance in the central area of the ns-Au film (see **Figure 2**a). This is presumably due to film morphology modifications induced by the heating caused by the forming process: we already reported that heat promotes dewetting phenomena and ns-Au thin films reorganization.[36,42] This leads to a decrease of the coverage,[36] thus causing a reduced contribution of Au (poorly emissive[60]) and an increased contribution of glass (highly emissive, roughly $\varepsilon = 0.8$) to the radiance. On the right of Figure 2a, atomic force microscopy (AFM) images of the ns-Au thin films, before and after the forming process, are reported. The reorganization of the gold thin films, at the nano and mesoscale, is noticeable. Specifically, the network undergoes an increase of a factor of 2 in cluster size, with the main peak shifting from 6 to ≈11 nm, as demonstrated by X-ray Diffraction (XRD) measurements published in ref. [36]. Furthermore, a mesoscale reorganization of the network, principally driven by dewetting and electroforming processes,[36] is evidenced by the change in the root-mean square roughness (Rq) of the film, as calculated from AFM images: Rq increases from about 3 to 6 nm.

The consequence of these effects is to produce an increase in the emissivity (see Figure 2a) and concurrently a decrease in reflectivity (according to Kirchhoff law[50]) of the physical systems (see also Figure S1, Supporting Information). Regarding the contribution of Au, we stress that also the modification of ns-Au morphology at the nanoscale over the entire sample[36] can lead to a change in optical properties in the long-wave infrared spectrum, as pointed out in ref. [61]. It turns out to be challenging to obtain a reliable estimation of ns-Au emissivity. The IR radiation detected by the camera is produced by both the nanostructure and the substrate, and it is difficult to disentangle the two contributions. The interfaces between different materials play also a role, along with reflections, in determining IR optical properties

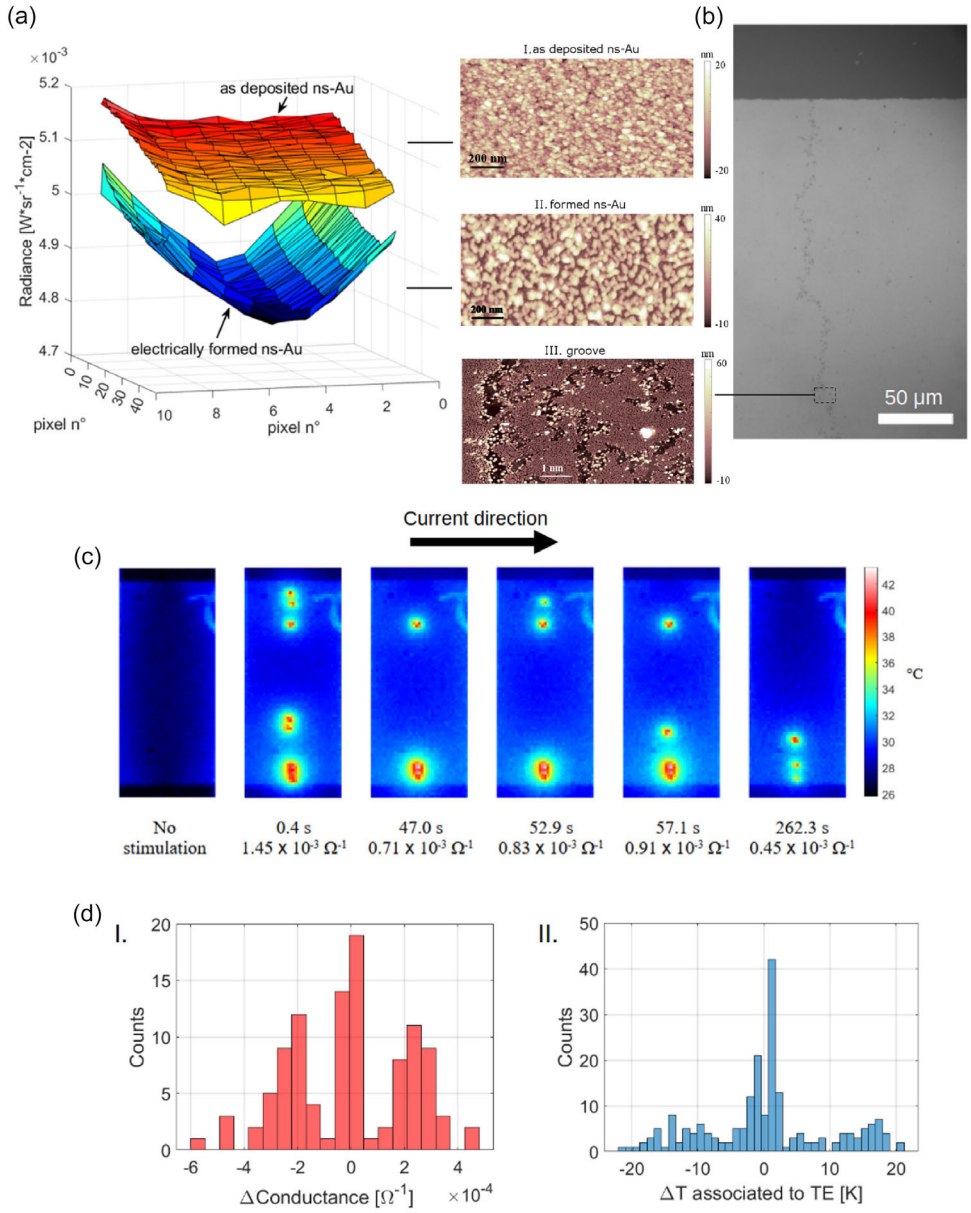

Figure 2. a) Radiance recorded from the as-deposited ns-Au sample and after the forming process. On the right, AFM images of the ns-Au thin films, (I) before and (II) after the forming process. An AFM image, magnification of the region interested by the groove, is shown at the bottom (III). b) Optical image of the groove, arising perpendicularly to current direction during the forming process. c) IR images of ns-Au film in five different instants of the recording, after the forming process. The connectivity changes during the stimulation, and different hotspots are immediately detectable. The applied bias is 3 V. d) Histogram of the variations in conductance (I) due to RS, detected by means of SMU, and associated variations in local temperature due to all TEs (II), as detected from the ns-Au sample using the thermal camera. Data are recorded during stimulation at 3 V.

of the physical system.[35] To obtain reliable temperatures measurements, we simply estimated the emissivity of the overall ns-Au/glass system after the forming process, by using the direct method.[62] We found an emissivity value between 0.65 and 0.70, in good agreement with the theoretical value found using the model in ref. [36], i.e., the mean of substrate emissivity and theoretical ns-Au emissivity, weighted for respective coverages.

We obtained the evidence from thermal images that conduction in ns-Au is no more uniform after forming completion. In particular, some hotspots are clearly detectable in thermal images during conduction (see Figure 2c) and from an optical inspection it is evident that a "groove" is often present along the deposit after forming, with its magnified view shown in the bottom AFM image of Figure 2a and the full view displayed in the optical image in Figure 2b. The groove preferentially forms in the central region of the film, where the highest temperature is reached, leading to the most significant morphological changes driven by both Joule heating and electromigration effects.

The groove is thus one of the main responsible for resistance increase that has been always reported after forming, along with the reorganization of the network morphology and connectivity over the entire nanostructured sample.[36] Evidences of the reorganization of the thin film during the forming process, at the nano and mesoscale, have also been provided by SEM and HR-TEM characterization.[36,42]

3.2. Pairwise between Resistive Switching and Local Thermal Events

The spatial distribution of the hotspots detected after the forming process by the thermal differential video (as the frame shown in Figure 2c) was concentrated in correspondence of the groove. This highlights the presence of different conductive pathways responsible of resistive switching activity along the inhomogeneous region that act as a "bottleneck", where current density is consistently higher than the surroundings, leading to important joule heating and electromigration effects, as pointed out in ref. [40].

Hotspots always presented a sharp peak of temperature in correspondence of few pixels (Figure 2c). Since our spatial resolution was limited to micrometric scale (see M&M), and due to the broadening effect caused by heat diffusion, it is difficult to provide a reliable estimation of the actual diameter of the region interested by RS events. However, in most cases, it is possible to indicate an upper bound for this quantity, i.e., camera Measurement Field of View (MFOV) = 3*IFOV $\approx$75 μm. We have often observed a sharp peak in temperature in correspondence to a single pixel, so it is possible that the actual diameter of the region interested in RS phenomena may be smaller than IFOV = 25 μm.

Interestingly, we find that TEs and EEs are essentially pairwise synchronized: almost every detected local TE happened concurrently to an EE recorded as network electrical activity by the gold electrodes, thus proving that TE were linked to RS and identified with a local (tens micrometers large) active site (see **Figure 3**a). Due to the evidence of the presence of localized ASs, we used micro-thermography to track the RS activity in different locations of the sample, i.e., to disentangle the contributions from different ASs. We exploit the fact that the areas of the sample undergoing strong temperature variations are easily detectable in PCs, to identify ASs locations. Then, we built time series of TEs associated with single ASs considering only TEs whose peak belongs to centers first or second nearest neighbors (Figure 3a). Time series associated to TEs recorded by different ASs will be further analyzed in the next paragraphs.

We stimulated ns-Au thin film for 5 min with different biases to trigger RS events. RS turns out to require a voltage threshold to be activated, that was found between 1 and 2 V. According to our findings RS is a threshold-activated phenomenon, similarly to analogous systems.[27,63] We have also performed electrical characterizations at higher voltages (3 V), also reversing the bias at each step. We show in Figure 2d the histograms of both the temperature and the electrical conductance variations detected, for a representative ns-Au sample at constant bias (3 V). Most of the conductance variations due to the exploration of different resistive levels produced multimodal and symmetric features in the resistance histogram, that are present also in the temperature histogram, highlighting preferred ways for the network to structurally and electrically reorganize. This is a consequence of heating and cooling of the same ASs in multilevel RS.[27] Even if the maximum temperature recorded over an AS is in the order of few tens degrees Celsius above room temperature, it is likely that the actual temperature reached by an AS is substantially higher but cannot be measured essentially due to limitation in spatial resolution.

A further increase in the voltage applied has often led to explore more frequently high resistance states (10^6–10^9 Ω), where hotspots are no longer detectable, suggesting the predominance of different conduction mechanisms that due to extremely low currents were not suited to be characterized with micro-thermography.

In Figure 3b,c, we show the comparison of the time series of the detected EEs and TEs, for two different biases, i.e., 2 and 3 V: by increasing voltage more RS events were triggered, and the activity tended to be more pronounced at the beginning of the stimulation, suggesting a nonstationary process.

3.3. Temporal and Spatial Distribution of Active Sites

Electric RS consists of local rearrangements of grain boundaries in the ns-Au sample, and concurrently, in local heating (or cooling) of the sample in the specific regions in which the rearrangement principally happened. Regions in the real-time series that underwent temperature variation were easily detected by PCA, because they were responsible for the major amount of variance in the dataset. If RS was triggered, the number of principal components (PCs) that accounted for larger amount of explained variance in the dataset of 15 000 recorded frames (5 min of electric stimulation), was of the order of few units (usually in the order of ten). This highlights the presence of few preferred configurations in electric conduction, each characterized by a different set of conductive ASs, confirming the major distribution of TEs close to the groove formed during the forming process.

Being the groove roughly perpendicular to current flow, our observations suggest that ns-Au multilevel RS was mainly linked to the formation and destruction of conductive paths in parallel. This finding is particularly significative because it highlights an important difference between ns-Au films and nanowires assemblies, where stimulation often led to winner takes all dynamics,[35,64] i.e., the tendency to reinforce a single conductive path. Furthermore, this fact accounts for nonlocal interactions between different regions of the thin film and spatial correlation, which can be exploited for data processing applications.[19,20]

First, it is evident that the number of ASs is much less than the amount of TEs (see Figure S2, Supporting Information). In 5 min of recordings, we have usually observed the presence of less than ten ASs, while at bias >1 V it is common to observe tens or hundreds of TEs. This implied the ASs formed recurrently in the same position. Furthermore, switching activity is not evenly distributed in time over all the ASs: some of them present a richer temporal activity and much higher number of TEs respect to others, that are rarely triggered.

We characterized the temporal distribution of TEs for each single ASs, following the procedure summarized in the previous paragraph. We found that strong temporal correlation is present in the TEs traces related to specific AS (see Figure S3, Supporting Information): it is common to observe periods ("bursts") of intense switching activity lasting several seconds, followed by

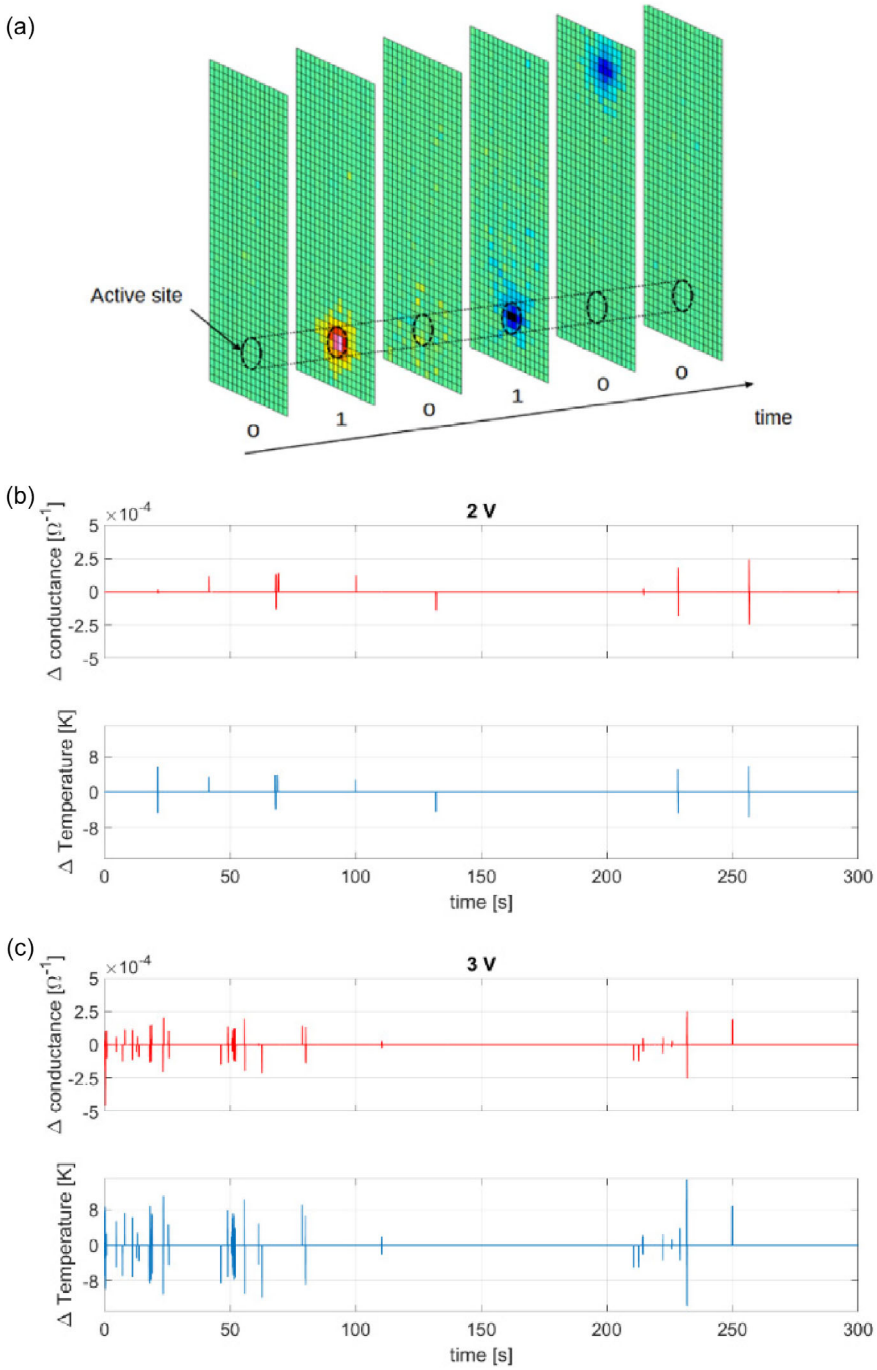

Figure 3. a) Schematic of the TE detection of in a single AS. After TEs detection, events were sorted based on their location, and binary time series for single ASs analysis were built. Frames where TEs are detected in correspondence to the chosen AS are associated with Boolean 1, all the others are associated with Boolean. b,c) Conductance variations associated with detected EEs (red), and temperature variations associated with TEs (blue) for two applied biases, (b) 2 V and (c) 3 V, respectively.

long periods of quiescence, as in in vitro single neuron recordings.[65] We performed TEs temporal analysis for ASs where a statistically significant number of event (>20) was detected.

To quantify more precisely the characteristic time scale that drove TEs in single ASs, burst detection was carried out by the self-adaptive method proposed in ref. [66]. Mean burst duration was estimated to range between hundreds of milliseconds to seconds. The mean ISI inside bursts was then computed and turned out to be of the order of few hundred milliseconds. These findings are summarized in Figure S3, Supporting Information where the joint ISI distribution is displayed, along with mean burst duration and mean ISI inside bursts.

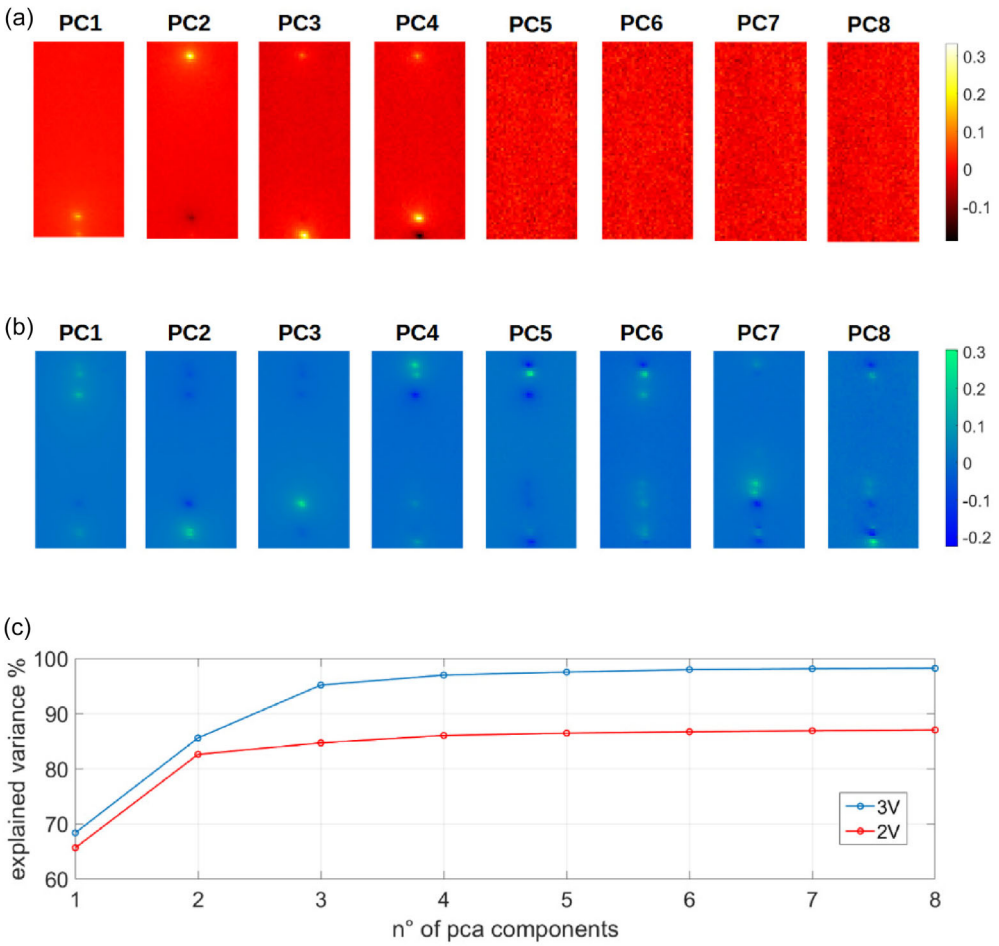

Figure 4. a) Illustrative case of the first eight PCs in the dataset of the thermal images acquired with bias equal to 2 V and b) 3 V (same of Figure 3). PC modulus is normalized and dimensionless. ASs are easily detectable in the first components. c) Percentage of cumulative explained variance for each PC.

In **Figure 4**, we reported the results of applying PCA on the thermal time series acquired under different biases (2 and 3 V). PCA turned out to be an effective method to resolve the local regions responsible for RS activity. The larger amount of variance was explained by the first ten components or less (Figure 4c), where ASs are easily detectable. From the comparison of the analysis in Figure 4a,b, it is possible to notice that increasing the applied bias RS activity can be triggered in more ASs. Notice that due to both the AS coordination and the nontrivial distribution of the experimental points (see the discussion in Section 2), some ASs were present in more than one PC.

For voltages much higher than the upper bound of the present range (5 V or more), the current density is sufficient to break the conductive paths corresponding to all the ASs, and the sample tends to explore only a high resistance state (10^6–10^9 Ω), without any AS clearly detectable by means of micro-thermography.

3.4. Critical Dimensions

To verify the role of film dimensions in the emerging of the complex dynamics of ns-Au network, we produced nanostructured samples with different geometries at the micrometer scale. Both width and length were reduced to approach thermal camera MFOV. Two classes of samples, with reduced length or width (down to 125 μm) were fabricated. Keeping one of the two dimensions well above MFOV allowed to easily detect ASs and to study the effect of shrinkage along the separate directions.

In accordance with our previous findings, in all samples with small width (125 μm), only one or two ASs can be clearly detected (see **Figure 5**). In contrast, reducing samples length (125 μm) allows to maintain a higher quantity of ASs. These observations confirm that ASs usually do not rise in series. If enough space is provided perpendicularly to current flow, multiple ASs can emerge in parallel.

These classes of samples can be also easily distinguished by means of PCA: samples with length = 125 μm present a larger number of ASs (comparable with that of macroscopic samples, length = 1 mm, width = 2 mm), that led to a higher number of significant PCs. This is evident in the explained variance plot (see Figure 5c).

Concurrently, the electrical characteristics are different for the two classes of samples. In the first case (length 1 mm, width 125 μm), RS activity is still present but is rarer. In the second case (length 125 μm, width 2 mm), RS is much more common.

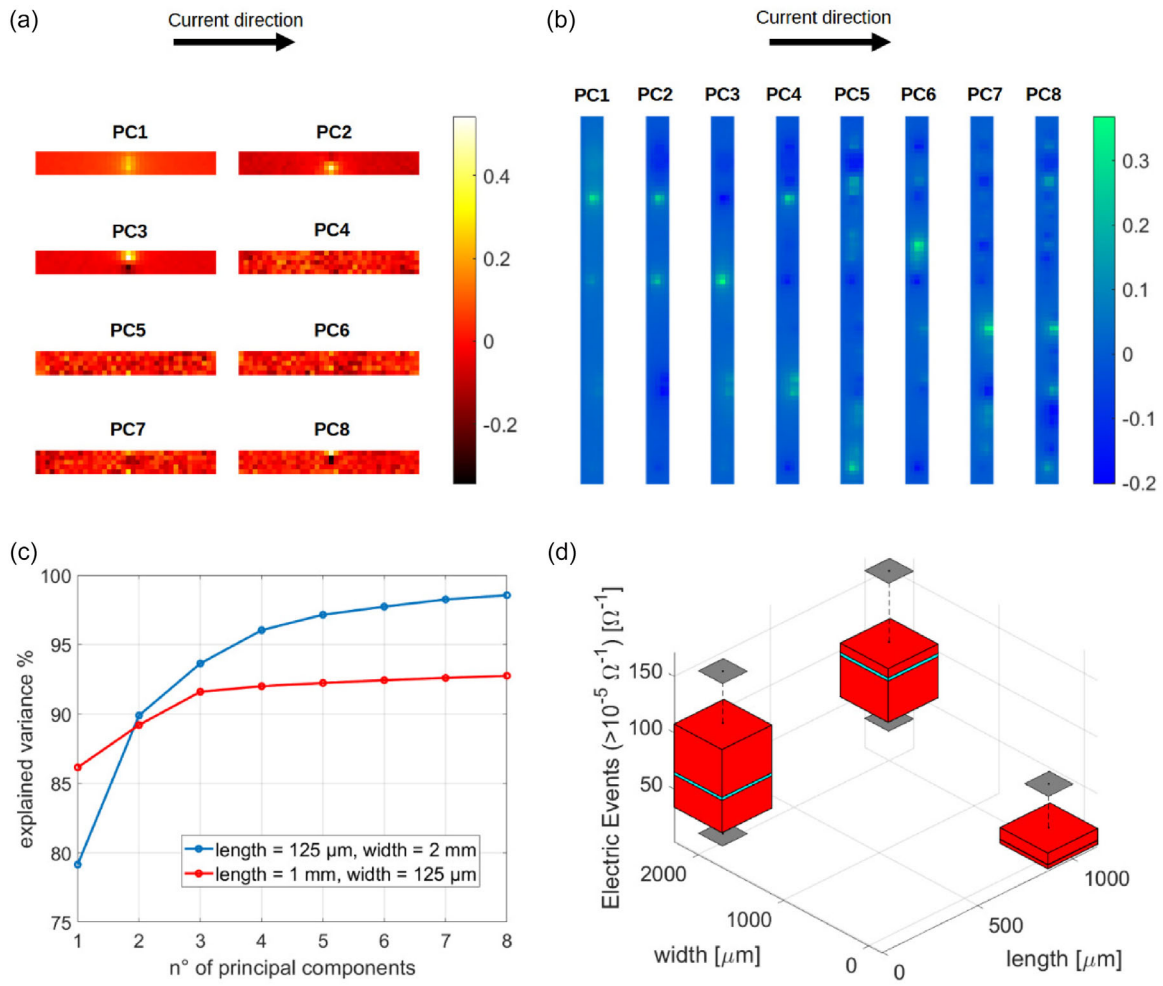

Figure 5. a) PCs of differential thermal images of a sample with length = 1 mm, width = 125 μm. Two ASs are clearly visible in the first three PCs. b) PCs of differential thermal images of a sample with length = 125 μm, width = 2 mm. c) Explained variance comparison. In the case of samples with length = 125 μm and width 2 mm, the explained variance per PC decreased slowly due to the more complex RS activity, i.e., higher number of ASs and TEs. d) Comparison between RS activity in samples with different geometries. Data were collected by applying ±3 V on three replicate samples, per each geometry. The red boxes and the gray planes represent the first and third quartiles, and the minimum and maximum values, respectively.

These results are expected since by reducing the width of the samples also the number of reconfigurable local regions available by current decreased (see also similar results in ref. [67]) and consequently a higher number of available ASs led to a richer phenomenology in electrical activity. To highlight this, in Figure 5d, we report the number of RS events for the three classes of samples that are the subject of the present work. For each sample, we reported the number of most significant events, i.e., the events with amplitude higher than $10^{-5}\,\Omega^{-1}$, that are also easily detectable by mean of thermal imaging.

3.5. Correlations in Network Activity

We also verified the presence of correlations between TEs taking place in different ASs. A measure of the possible interactions between TEs series is given by the STTC[53] (see Section 2).

RS does not exhibit complete stationarity, as required by STTC method, at least since the first ten seconds: immediately after the beginning of electric stimulation, RS events are more frequent than the rest of the measurements. After several tens of seconds, RS activity becomes stable, and silence periods of seconds or minutes arise, along with bursts. This fact suggests that the system underwent strong permanent modifications since a more stable configuration was reached. With the aim to disentangle these two dynamic regimes, and to work as far as possible in stationary regimes, we computed the STTC separately over the first minute and the last 4 min of the recordings. **Figure 6** reports the results of this analysis for a typical sample (length = 1 mm, width = 2 mm).

Interestingly, STTC showed high variability in ASs coordination. Some ASs present strong coordination on time scales typical of inter-burst activity (i.e., for synchronicity windows smaller than 1 s). For other pairs of active sites, ASs tend not to be coordinated on these time scales. In this second scenarios, significant increase in STTC is obtained only by increasing the synchronicity window to the order of seconds, or tens of seconds. From the collected data, it is not possible to identify a typical distance

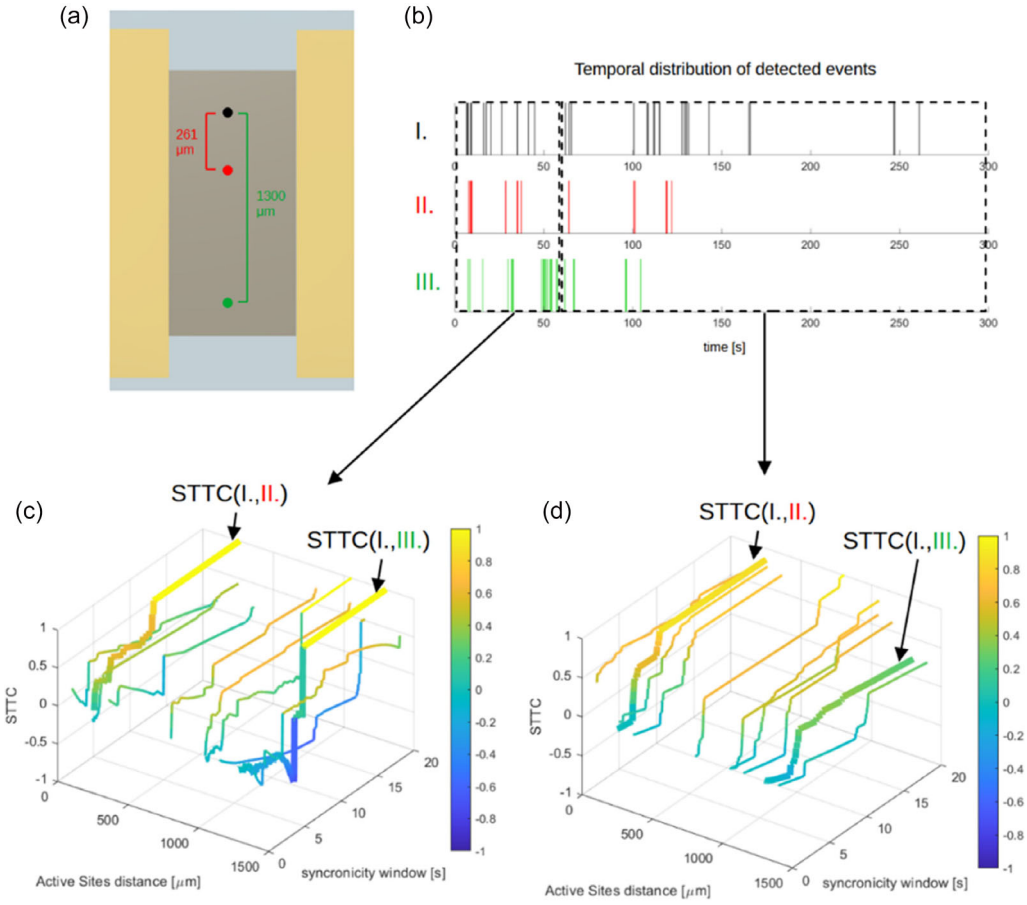

Figure 6. Illustrative example of STTC coefficients, computed for different values of the synchronicity window and distances between ASs. a) Schematics of the disposition of three ASs along the sample. b) Binarized recordings of the TEs in the ASs in (a). STTC computed for c) the first minute of recording (interval from 0 to 60 s) and d) the last 4 min (interval from 60 to 300 s). STTCs computed on traces I/II and I/III are emphasized. The applied bias is −3 V.

leading ASs to produce coordinated activity (Figure 6), since coordination can arise at very different scales (also in ASs several hundred micrometers apart). From STTC analysis, we can deduce that closest ASs show correlated activity for a longer period of time (Figure 6d), while correlated activity on shorter period (Figure 6c) can be reached even for ASs far apart, depending on network connectivity.

Despite ASs tend to be located near the groove, the morphological modifications due to dewetting during the forming process take place in most of the ns-Au films, leading to further complex connectivity of the network that in turn promotes ASs to effectively interact over long distances. In this picture, a RS event taking place in an ASs leads to a current redistribution inside the network that can trigger further RS events in the other distant ASs. Considering device-device variability and several measurements at 3 V, we have always observed the reduction of the coordination between ASs during the last 4 min of recording (Figure 6d).

Interestingly, we found that the applied bias can partially control the degree of coordination between ASs. When a RS event happens with low bias, the redistributed current is not sufficient to trigger further RS events in the neighboring sites, and the degree of coordination is lower than for higher bias applied (see **Figure 7**a,b for comparison). Film dimensions can also influence the coordination between AS's activity. Despite the number of them is much lower for narrower nanostructured film, their activity tends to be correlated (see Figure 7c).

We also computed the center of mass (CM) of the conduction map (see Supporting Information S4), to track a coarse-grained evolution of the conductance during repeated stimulations. We highlighted the presence of the initial chaotic transient, characterized by strong displacements of the CM, lasting several seconds, and the following stabilization in a preferred configuration of conducting ASs, with less frequent modifications of CM location. This fact highlights that after the transient occurring at the beginning of a stimulation by a constant bias, ASs reach a more stable configuration and are less prone to produce RS events in response to current redistribution across the network. In this phase, RS activity is much more linked to single ASs that produced bursts locally, with less influences between spatially separated regions, similarly to single-neuron spiking behavior highlighted in ref. [63].

In a biological context, coordination between neural spike trains is thought to play a key role in information propagation and processing, as also in self-organization of the neural system during development.[68,69] For instance, in spontaneous retinal

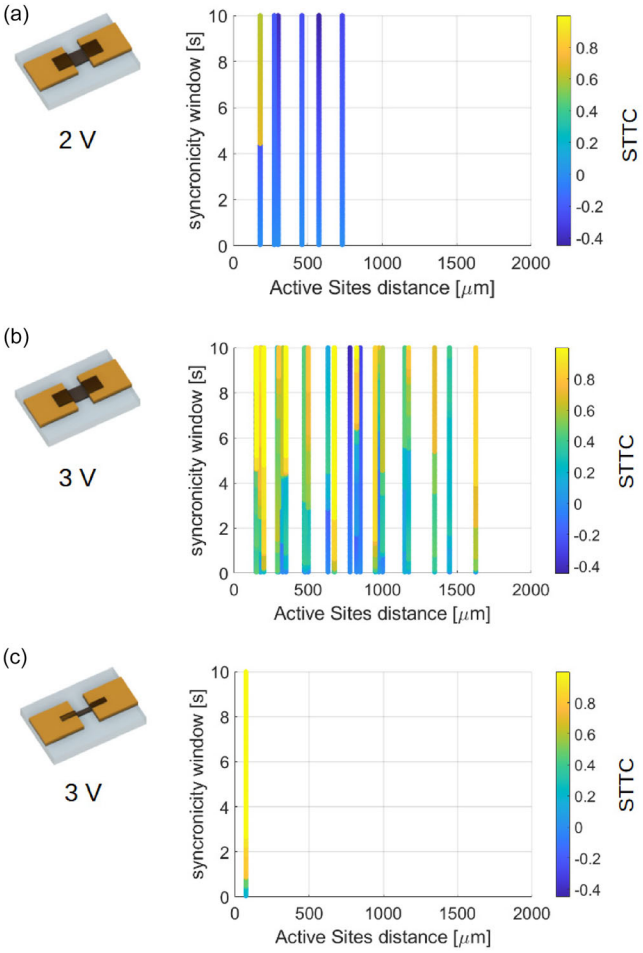

Figure 7. STTC computed in the first minute of recording for a sample with length = 1 mm, width = 2 mm at a) −2 V and b) −3 V, and for a microfabricated sample with c) length = 1 mm and width = 125 μm.

activity, the propensity of two neurons to fire close in time to each other can affect their wiring onto a common target.[70] In a non-biological context, and specifically in our nanostructured system, STTC is a suitable method to describe the dynamics of the system, independent on the firing rate, and to suggest the presence of a certain degree of correlations in the network, i.e., the presence of interactive regions. Further studies are needed to evaluate the entity of these network's interactions, eventually the formation of recurrent loops and feedback regions in different sites of the nanostructured network.

3.6. Control of the Network Connectivity

Despite resistive switching is an intrinsically stochastic phenomenon, we explored the response of ns-Au thin film to pulsed stimuli to effectively tune the electrical response and conductive pattern. The deterministic part in the electric response is particularly interesting from a fundamental point of view, due to the possibility to explore information mapping in a physical substrate (i.e., a sort of engram),[71] and in view of future implementation of programming protocols of data processing systems based on ns-Au devices, such as for reconfigurable threshold logic gates.[20,21]

It is straightforward to understand that by applying sufficiently high voltages all the conductive connections are broken, and the sample goes to a high resistive state (HRS) (i.e., electrical resistance > MΩ), in which no ASs are detectable due to thermal camera sensitivity. However, smaller biases are likely to reform the conductive paths, allowing the sample to switch to a low resistance state (LRS), in the order of kΩ.

To study the effect of pulsed electrical stimulation, we applied the following experimental routine: 1) five pulses with amplitude 6 V and duration 250 ms, to drive the sample to the HRS (Reset); 2) thirty pulses with amplitude 2.5 V and duration 250 ms, to switch the sample back to a LRS (Set). For the Set operation, two different protocols were employed, unipolar train pulses and bipolar train pulses, i.e., all the pulses have the same polarity (opposite to the Reset pulses), or every pulse has opposite polarity respect to the previous one (in **Figure 8** illustrative examples are shown). The reset operation (corresponding to HRS) allowed to repeat the Set operation multiple times starting from the same initial condition, i.e., no conductive path formed inside the sample. The two different Set protocols were tested on the same sample.

We observed that by applying unipolar trains of pulses there is a low probability to trigger the formation of new conductive paths (Figure 8b). To the contrary, a continuous change in the polarity of the pulse train is way more effective in forming many connections. In fact, by applying alternate pulse trains an increasingly high number of conductive paths is formed and present RS activity during the stimulus application (Figure 8c). This change in conductive pattern is reversible and reproducible, as the conductive patterns reported in Figure 8 are consecutive in time (see also connectivity changes after further repetitions of pulsed stimuli reported in Figure S5, Supporting Information, performed again on the same sample whose results are shown in Figure 8). We tested five samples with width = 2 mm to exploit our spatial resolution looking at larger devices, and even if device-device variability is present in terms of number of conductive paths and easiness to trigger their activation, this same phenomenology was observed irrespective of the sample length.

An analogous phenomenology, along with the possibility of reliably change the electric conductance of the system, was reported in multiple nanogap-based devices,[72] and it is likely that the physical origin of RS in the systems under study was similar to the one reported in the latter, i.e., atom surface diffusion and field migration. In our case, the formation of conductive hillocks/filaments sustaining high current densities (and consequently, prone to the structural modifications due to electromigration and joule heating) accounted also for the emerging of the hotspots described in Figure 2, with high IR contrast respect to the surroundings.

The control over the network connectivity and its reprogrammability enables the tuning of the conductivity map of the nanostructured system. The emergence of new micrometric active sites defines different resistance states of the overall system, as recorded by two electrodes and stressed in the conductance distributions reported on the right of Figure 8b,c.

The controllability over connectivity, and therefore over the resistance states of the system, is important for all those data

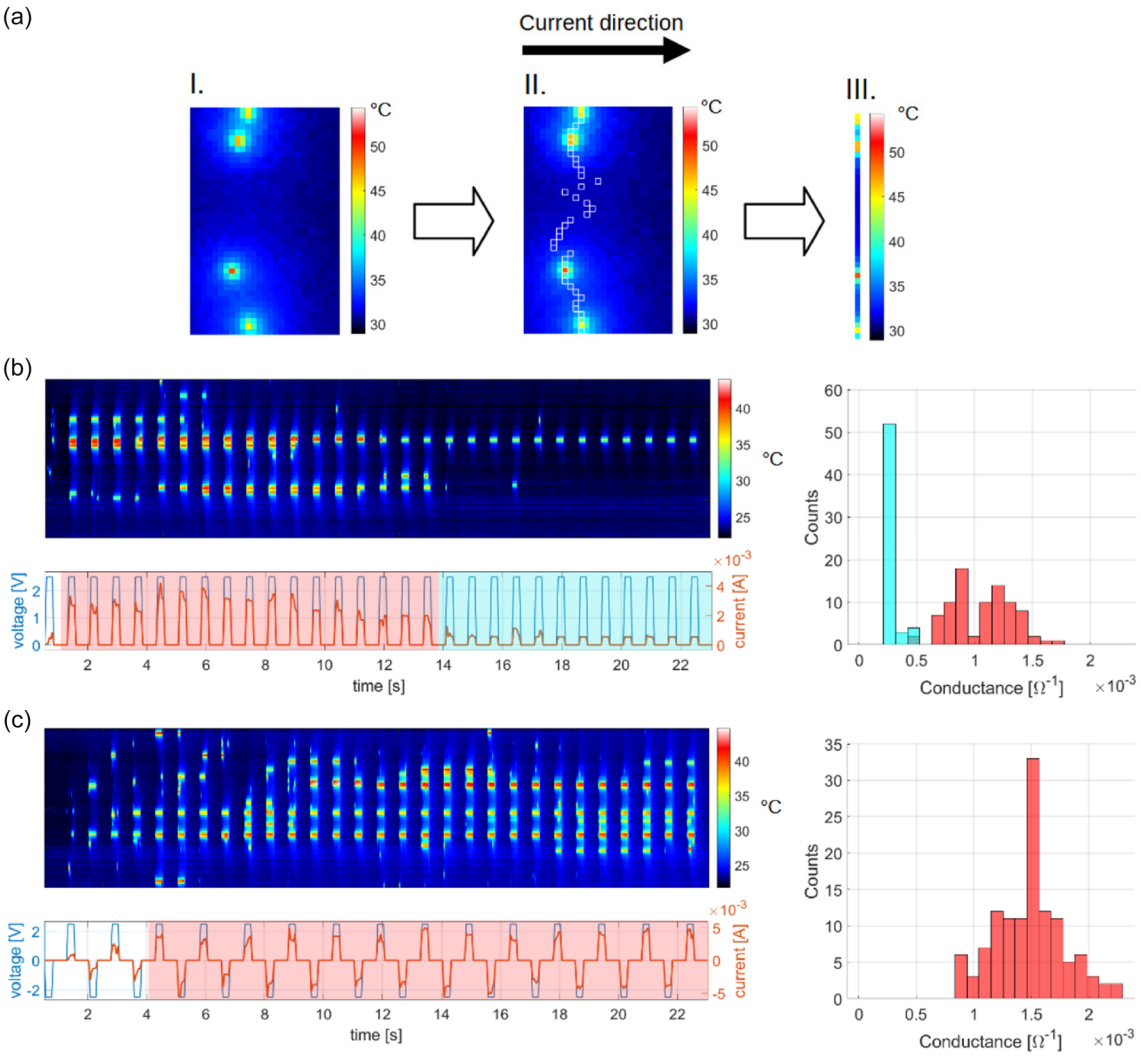

Figure 8. a) Construction of the time series representative of the conductance evolution: for each frame (I), we detect the maxima per each row of pixels parallel to the current direction (white squares) (II), and these are used to build a 1D array of pixels representative of the conduction state of the sample. In this way, it is possible to follow the evolution of the conduction of the sample during the electrical stimulation using a single 2D image. b,c) Evolution of conductance of a gold nanostructured sample due to different pulsed stimulation. We applied two different train pulses protocols; namely, (b) unipolar trains pulse and (c) alternate train pulse. On the right, the corresponding distributions of the absolute conductance values recorded from the ns-Au sample during the writing pulses. The sample has length = 125 μm, width = 2 mm.

processing applications in which different resistance levels are needed. For instance, this capability is essential for the implementation of programmable analog circuits, as gain amplifiers and relaxation oscillators, where variable resistances composed by cluster-assembled nanostructures have been integrated in hybrid computing platforms with conventional components.[73]

The controllability on specific connectivity and resistivity maps has direct implications also for nonlinear threshold logic gates based on cluster-assembled materials.[20,21,74] Specifically, in reconfigurable nonlinear threshold logic gates the weights associated to the inputs are input-dependent, as introduced by the Receptron model.[75] In this nanostructured hardware, the nonlinear dependence of the weights by the inputs is implemented by the complex connectivity of the network and the resulting conductivity map.[71] Therefore, the ability to control the network connectivity significantly impacts the device's capacity to explore a wide range of weight configurations, which is essential for implementing a broad set of Boolean functions.

Furthermore, the control over the dynamic of the system, in terms of synchronicity and correlated activity of its local active sites, can be exploited for the processing of time-series, with the methodology used in ref. [76].

4. Conclusion

We experimentally demonstrated the role of network reorganization at different scales in the emerging of nonlinear electrical responses of self-assembled Au nanostructured films. In particular, the presence of localized micrometric areas that are

responsible for the RS activities (i.e., ASs), related to local rearrangement of grain boundaries at the nanoscale, has been deeply characterized.

The combined use of micro-thermography and PC analysis has been proved as a nonperturbative method to map electric conduction dynamic in ns-Au thin films, and we effectively applied it to study the spatial and temporal correlations in RS activity of a nanostructured resistive switching films. Furthermore, we identified the role of the dimensionality of the system in RS dynamic.

RS activity may emerge from the organization of micrometric active sites in the nanostructured network in correlated activity, by following simple constraints on distance-based connectivity as biological neural systems, as also by a complex connectivity which links remote regions of the network. By changing the dimension of the nanostructured network and the bias applied it is possible to control at a certain degree the synchronicity and correlation in the activity of the network, as also the number of active sites. This result suggests that nanostructured Au films are interesting platforms to study interacting and recurrent electrical activity typical of neuronal systems. The methodology developed, sourced by neuroscience and biology framework, is an important tool for the characterization of all those self-assembled systems showing neuromorphic properties.

The controlled and reversible programmability of the ns-Au network's connectivity, by means of specific train pulses used as writing stimuli, demonstrated the capability of our devices to encode stimuli into specific connectivity, which can last in time and be reprogrammed on demand multiple times. This enables the fabrication of data processing devices based on self-assembled systems, such as reconfigurable threshold logic gates,[20,21] featuring tailored and adaptable connectivity that allows controlled emergent analog responses in complex networks.

Supporting Information

Supporting Information is available from the Wiley Online Library or from the author.

Conflict of Interest

The authors declare no conflict of interest.

Data Availability Statement

The data that support the findings of this study are available from the corresponding author upon reasonable request.

Keywords

adaptive connectivity, correlation coefficient, critical dimensions, micro-thermography, nanostructured network

Received: May 21, 2025
Revised: August 12, 2025
Published online: September 13, 2025

[1] A. Elliott, *The Culture of AI: Everyday Life and Digital Revolution*, Taylor & Francis Group, London **2019**.
[2] R. Comolatti, A. Pigorini, S. Casarotto, M. Fecchio, G. Faria, S. Sarasso, M. Rosanova, O. Gosseries, M. Boly, O. Bodart, et al., *Brain Stimulat.* **2019**, *12*, 1280.
[3] B. Dresp-Langley, *Big Data Cogn. Comput.* **2020**, *4*, 10.
[4] O. Sporns, G. Tononi, R. Kötter, *PLoS Comput. Biol.* **2005**, *1*, e42.
[5] B. B. Averbeck, P. E. Latham, A. Pouget, *Nat. Rev. Neurosci.* **2006**, *7*, 358.
[6] X. Jia, W. Shao, N. Hu, J. Shi, X. Fan, C. Chen, Y. Wang, L. Chen, H. Qiao, X. Li, *Front. Neurosci.* **2022**, *16*, 854199.
[7] M. B. Feller, *Neuron* **1999**, *22*, 653.
[8] A. G. Blankenship, M. B. Feller, *Nat. Rev. Neurosci.* **2010**, *11*, 18.
[9] L. A. Kirkby, G. S. Sack, A. Firl, M. B. Feller, *Neuron* **2013**, *80*, 1129.
[10] V. Pasquale, P. Massobrio, L. L. Bologna, M. Chiappalone, S. Martinoia, *Neuroscience* **2008**, *153*, 1354.
[11] E. Persi, D. Horn, V. Volman, R. Segev, E. Ben-Jacob, *Neural Comput.* **2004**, *16*, 2577.
[12] N. Raichman, E. Ben-Jacob, *J. Neurosci. Methods* **2008**, *170*, 96.
[13] D. A. Wagenaar, J. Pine, S. M. Potter, *BMC Neurosci.* **2006**, *7*, 11.
[14] D. Lonardoni, H. Amin, S. Di Marco, A. Maccione, L. Berdondini, T. Nieus, *PLoS Comput. Biol.* **2017**, *13*, e1005672.
[15] T. Nieus, V. D'Andrea, H. Amin, S. Di Marco, H. Safaai, A. Maccione, L. Berdondini, S. Panzeri, *Sci. Rep.* **2018**, *8*, 5578.
[16] S. K. Bose, C. P. Lawrence, Z. Liu, K. S. Makarenko, R. M. J. Van Damme, H. J. Broersma, W. G. Van Der Wiel, *Nat. Nanotechnol.* **2015**, *10*, 1048.
[17] G. Milano, G. Pedretti, K. Montano, S. Ricci, S. Hashemkhani, L. Boarino, D. Ielmini, C. Ricciardi, *Nat. Mater.* **2022**, *21*, 195.
[18] A. Loeffler, A. Diaz-Alvarez, R. Zhu, N. Ganesh, J. M. Shine, T. Nakayama, Z. Kuncic, *Sci. Adv.* **2023**, *9*, eadg3289.
[19] M. Mirigliano, B. Paroli, G. Martini, M. Fedrizzi, A. Falqui, A. Casu, P. Milani, *Neuromorph. Comput. Eng.* **2021**, *1*, 024007.
[20] G. Martini, M. Mirigliano, B. Paroli, P. Milani, *Jpn. J. Appl. Phys.* **2022**, *61*, SM0801.
[21] F. Borghi, T. R. Nieus, D. E. Galli, P. Milani, *Front. Neurosci.* **2024**, *18*, 1465789.
[22] A. Vahl, G. Milano, Z. Kuncic, S. A. Brown, P. Milani, *J. Phys. Appl. Phys.* **2024**, *57*, 503001.
[23] G. Milano, G. Pedretti, M. Fretto, L. Boarino, F. Benfenati, D. Ielmini, I. Valov, C. Ricciardi, *Adv. Intell. Syst.* **2020**, *2*, 2000096.
[24] Z. Kuncic, T. Nakayama, *Adv. Phys. X* **2021**, *6*, 1894234.
[25] N. Carstens, B. Adejube, T. Strunskus, F. Faupel, S. Brown, A. Vahl, *Nanoscale Adv.* **2022**, *4*, 3149.
[26] M. D. Pike, S. K. Bose, J. B. Mallinson, S. K. Acharya, S. Shirai, E. Galli, S. J. Weddell, P. J. Bones, M. D. Arnold, S. A. Brown, *Nano Lett.* **2020**, *20*, 3935.
[27] M. Mirigliano, D. Decastri, A. Pullia, D. Dellasega, A. Casu, A. Falqui, P. Milani, *Nanotechnology* **2020**, *31*, 234001.
[28] M. López-Suárez, C. Melis, L. Colombo, W. Tarantino, *Phys. Rev. Mater.* **2021**, *5*, 126001.
[29] W. Tarantino, L. Colombo, *Phys. Rev. Res.* **2020**, *2*, 043389.
[30] R. K. Daniels, J. B. Mallinson, Z. E. Heywood, P. J. Bones, M. D. Arnold, S. A. Brown, *Neural Networks* **2022**, *154*, 122.
[31] F. Michieletti, D. Pilati, G. Milano, C. Ricciardi, *Adv. Funct. Mater.* **2025**, *35*, 2423903.
[32] D. Pilati, F. Michieletti, A. Cultrera, C. Ricciardi, G. Milano, *Adv. Electron. Mater.* **2024**, *10*, 2400750.
[33] A. Cultrera, G. Milano, N. De Leo, C. Ricciardi, L. Boarino, L. Callegaro, *Sci. Rep.* **2021**, *11*, 13167.
[34] G. Milano, A. Cultrera, L. Boarino, L. Callegaro, C. Ricciardi, *Nat. Commun.* **2023**, *14*, 5723.

[35] Q. Li, A. Diaz-Alvarez, R. Iguchi, J. Hochstetter, A. Loeffler, R. Zhu, Y. Shingaya, Z. Kuncic, K. Uchida, T. Nakayama, *Adv. Funct. Mater.* **2020**, *30*, 2003679.
[36] G. Nadalini, F. Borghi, T. Košutová, A. Falqui, N. Ludwig, P. Milani, *Sci. Rep.* **2023**, *13*, 19713.
[37] K. Wegner, P. Piseri, H. V. Tafreshi, P. Milani, *J. Phys. Appl. Phys.* **2006**, *39*, R439.
[38] C. Minnai, *Nano Futures* **2018**, *2*, 011002.
[39] M. Mirigliano, F. Borghi, A. Podestà, A. Antidormi, L. Colombo, P. Milani, *Nanoscale Adv.* **2019**, *1*, 3119.
[40] M. Mirigliano, P. Milani, *Adv. Phys. X* **2021**, *6*, 1908847.
[41] F. Profumo, F. Borghi, A. Falqui, P. Milani, *J. Phys. Appl. Phys.* **2023**, *56*, 355301.
[42] A. Casu, A. Chiodoni, Y. P. Ivanov, G. Divitini, P. Milani, A. Falqui, *ACS Appl. Nano Mater.* **2024**, *7*, 7203.
[43] M. López-Suárez, C. Melis, L. Colombo, W. Tarantino, in *2023 IEEE Nanotechnology Materials and Devices Conference*, Paestum (Salerno), Italy, October **2023**.
[44] E. Barborini, P. Piseri, P. Milani, *J. Phys. Appl. Phys.* **1999**, *32*, L105.
[45] C. Chiappini, P. Piseri, S. Vinati, P. Milani, *Rev. Sci. Instrum.* **2007**, *78*, 066105.
[46] P. Piseri, H. V. Tafreshi, P. Milani, *Curr. Opin. Solid State Mater. Sci.* **2004**, *8*, 195.
[47] F. Borghi, M. Mirigliano, D. Dellasega, P. Milani, *Appl. Surf. Sci.* **2022**, *582*, 152485.
[48] F. Borghi, M. Mirigliano, C. Lenardi, P. Milani, A. Podestà, *Front. Chem.* **2021**, *9*, 619432.
[49] T. N. Narasimhan, *Rev. Geophys.* **1999**, *37*, 151.
[50] M. Vollmer, K.-P. Möllmann, *Infrared Thermal Imaging: Fundamentals, Research and Applications*, 2nd ed., Wiley-VCH Verlag GmbH & Co. KGaA, Weinheim, Germany **2018**.
[51] J. Lever, M. Krzywinski, N. Altman, *Nat. Methods* **2017**, *14*, 641.
[52] A. L. Pomerantsev, *Chemometrics in Excel*, 1st ed., Wiley **2014**.
[53] C. S. Cutts, S. J. Eglen, *J. Neurosci.* **2014**, *34*, 14288.
[54] D. Cabrera-Garcia, D. Warm, P. de la Fuente, M. T. Fernández-Sánchez, A. Novelli, J. M. Villanueva-Balsera, *Sci. Rep.* **2021**, *11*, 20407.
[55] M. Chini, T. Pfeffer, I. Hanganu-Opatz, *eLife* **2022**, *11*, e78811.
[56] H. Roh, S. Kim, H.-M. Lee, M. Im, *Sci. Rep.* **2024**, *14*, 29623.
[57] D. P. Hunley, S. L. Johnson, R. L. Flores, A. Sundararajan, D. R. Strachan, *J. Appl. Phys.* **2013**, *113*, 234306.
[58] O. M. G. Ward, E. McCann, *J. Phys. Appl. Phys.* **2021**, *54*, 475303.
[59] F. Léonard, *Appl. Phys. Lett.* **2011**, *98*, 103101.
[60] S. Edalatpour, M. Francoeur, *J. Quant. Spectrosc. Radiat. Transf.* **2013**, *118*, 75.
[61] V. A. Golyk, M. Krüger, M. Kardar, *Phys. Rev. E* **2012**, *85*, 046603.
[62] C. Zhu, M. J. Hobbs, J. R. Willmott, *Meas. Sci. Technol.* **2020**, *31*, 044007.
[63] S. K. Acharya, E. Galli, J. B. Mallinson, S. K. Bose, F. Wagner, Z. E. Heywood, P. J. Bones, M. D. Arnold, S. A. Brown, *ACS Appl. Mater. Interfaces* **2021**, *13*, 52861.
[64] H. G. Manning, F. Niosi, C. G. Da Rocha, A. T. Bellew, C. O'Callaghan, S. Biswas, P. F. Flowers, B. J. Wiley, J. D. Holmes, M. S. Ferreira, et al., *Nat. Commun.* **2018**, *9*, 3219.
[65] A. Mazzoni, F. D. Broccard, E. Garcia-Perez, P. Bonifazi, M. E. Ruaro, V. Torre, *PLoS One* **2007**, *2*, e439.
[66] L. Chen, Y. Deng, W. Luo, Z. Wang, S. Zeng, *Prog. Nat. Sci.* **2009**, *19*, 229.
[67] Z. Heywood, J. Mallinson, E. Galli, S. Acharya, S. Bose, M. Arnold, P. Bones, S. Brown, *Neuromorph. Comput. Eng.* **2022**, *2*, 024009.
[68] M. Chiappalone, M. Bove, A. Vato, M. Tedesco, S. Martinoia, *Brain Res.* **2006**, *1093*, 41.
[69] N. Dehorter, L. Vinay, C. Hammond, Y. Ben-Ari, *Eur. J. Neurosci.* **2012**, *35*, 1846.
[70] M. B. Feller, *Neural Dev.* **2009**, *4*, 24.
[71] G. Milano, F. Michieletti, C. Ricciardi, E. Miranda, *Nat. Commun.* **2025**, *16*, 3509.
[72] Z. Tian, G. Yao, Z. Ren, D. Yu, J. Tian, M. Li, P. Peng, L. Ren, F. Liu, Y. Fu, *ACS Appl. Mater. Interfaces* **2024**, *16*, 26360.
[73] S. Radice, F. Profumo, F. Borghi, A. Falqui, P. Milani, *Adv. Electron. Mater.* **2024**, *10*, 2400434.
[74] B. Paroli, F. Borghi, M. A. C. Potenza, P. Milani (Preprint), arXiv:2506.19642, v1, Submitted: Jun. **2025**.
[75] B. Paroli, G. Martini, M. A. C. Potenza, M. Siano, M. Mirigliano, P. Milani, *Neural Networks* **2023**, *166*, 634.
[76] F. Profumo, F. Borghi, T. Angì, M. Maschietto, S. Vassanelli, P. Milani, *Adv. Intell. Syst.* **2025**, 2401150.